Composite Structures 324 (2023) 117550

Contents lists available at ScienceDirect

Composite Structures

journal homepage: www.elsevier.com/locate/compstruct

Butterfly lattice materials for controllable multi-stage energy absorption

Wu Yuan [a,b], Wenfeng Liu [c], Hongwei Song [a,b,*], Chenguang Huang [b]

[a] Key Laboratory for Mechanics in Fluid Solid Coupling Systems, Institute of Mechanics, Chinese Academy of Sciences, Beijing 100190, China
[b] School of Engineering Science, University of Chinese Academy of Sciences, Beijing 100049, China
[c] Institute of Physics, University of Amsterdam, Amsterdam, the Netherlands

ARTICLE INFO

Keywords:
Lattice material
Multi-stage crushing
Gradual energy absorption
Bending-dominated

ABSTRACT

Energy absorption properties of cellular materials have gained increasing interest due to their superior performance and immense design space. This paper introduces a novel lattice material with a Butterfly configuration that has controllable multi-stage crushing behavior and high specific energy absorption capacity. A theoretical model is developed to predict the plateau stress, elastic modulus and critical strain of each stage, in order to obtain the multi-stage stress-strain curve. Compression experiments and the finite element modelling are also carried out to validate the theoretical model. Theoretical and experimental results show that the Butterfly lattice material has more than two crushing stages and a specific energy absorption property comparable to the traditional stretching-dominated lattice material. Finally, effects of topology configuration, cell number, and geometrical parameter on the energy absorption behavior are analyzed. It is found that the length of the vertical beam dramatically influences the plateau load and deformation behavior of each stage.

1. Introduction

Crashworthiness has always been a severe concern for cellular materials and structures, which have many applications in aerospace, automobile, and packaging [1–7]. Light-weight lattice materials with high specific stiffness and specific strength properties are seen as one important cellular materials due to their high energy absorption capacity [8–11]. The stretching-dominated deformation behavior and their stiffness and strength scale linearly with their relative density $\overline{\rho}$. Thus, for a relative density of $\overline{\rho} = 0.1$ the stretching-dominated structure is about 10 times stiffer and 3 times stronger than bending-dominated structure[12,13]. A variety of lattice configurations have been proposed and produced such as tetrahedral[14], pyramidal[15], 3D Kagome[16], octet truss[13,17] and BCC/hourglass[18] lattice. The bending and stretching dominated lattices as well as their post-elastic performance has been deeply researched [19–21] and some theoretical model are also developed [22–24]. All of them exhibit much higher initial specific stiffness and strength than foams with the same relative density.

However, the initial yield of above stretch-dominated lattice of low relative density is usually followed by plastic buckling or brittle collapse of the beams, leading to dramatical post-yield softening [25,26]. This deformation behavior may cause a catastrophic failure of the structure, and result in a low specific energy absorption (SEA), which is defined as the energy absorption per volume or per unit mass. One of the helpful methods is to replace solid lattice with hollow members to solve this limitation [27,28]. The self-contact of the hollow lattice can suppress the post-yield softening phenomenon. The other method is increasing the lattice members in the loading direction, which is worked by contacting lattice members of the contiguous layers [29,30].

Another widely used strategy in the energy absorption system is the constant energy absorption (CEA) strategy for crashworthy designers. Bending-dominated foam and honeycomb materials are once seen as the ideal energy absorption materials due to their long, stable yield plateau stress during the bending process [31–33]. Low initial stiffness and strength of such materials can reduce the overload or accleration in an impact event, therefore reduce damages to the inner equipment or occupants. However, randomly distributed pore structures inside the foam material cause an uncontrollable mechanical property in the design step. Meanwhile, since the Young's modulus and initial yield strength of foams scale with relative density $\overline{\rho}$ in the form $\overline{\rho}^2$ and $\overline{\rho}^{\frac{3}{2}}$ respectively [15], the stiffness and strength of foams decrease rapidly with the decrease of the relative density, leading to pretty low energy absorption efficiency. The volume SEA and mass SEA of a pure bending-dominated

* Corresponding author at: Key Laboratory for Mechanics in Fluid Solid Coupling Systems, Institute of Mechanics, Chinese Academy of Sciences, Beijing 100190, China.
E-mail address: songhw@imech.ac.cn (H. Song).

https://doi.org/10.1016/j.compstruct.2023.117550
Received 14 May 2023; Received in revised form 11 August 2023; Accepted 6 September 2023
Available online 7 September 2023
0263-8223/© 2023 Elsevier Ltd. All rights reserved.

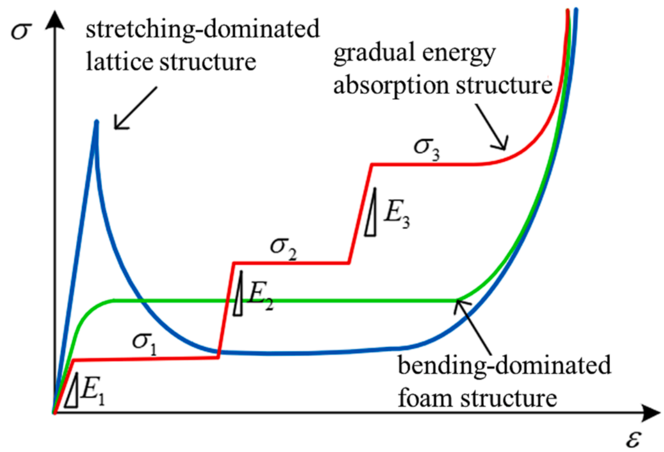

Fig. 1. The comparison of crushing behavior among the bending-dominated structures, stretch-dominated lattice structures, and multi-stage structures.

material scale with $\overline{\rho}^{\frac{3}{2}}$ and $\overline{\rho}^{\frac{1}{2}}$, respectively.

For crashworthiness, both the total quantity of the absorbed energy and the capacity to reduce the damage of the protected things have to be considered [34]. The CEA energy absorption structure cannot adept to various impact events and provide efficient protection. This limitation of manipulation appears in generating almost the same force corresponding to different the initial velocities, hence the only difference between different cases is larger stroke of deformation for larger applied kinetic energy amount [35]. An ideal energy absorption strategy aims at manipulating accidents feedbacks (reactions/damages) depending on accidents initial impact velocities. However, the stretching-dominated material's high initial strength damages the target because of its higher initial strength. The lower initial strength of the CEA strategy will reduce the total absorbed kinetic energy[36]. To solve this problem, Xu [37] et al. proposed a gradual energy absorption (GEA) strategy. The absorption system has different gradually increasing stiffness during the deformation process in the GEA strategy. This strategy was extended to various structures and applications by Esa [35] and Zahran [34], called the piecemeal energy absorption (PEA) strategy. The piecemeal strength of different levels was carried out by the nested round or square thin-walled tubes with different lengths and imperfections [38–42]. Figs. 1 and 2 show the three typical loading paths, materials and structures with different absorption strategies.

This work designs a novel three-dimensional lattice material capable of multi-stage deformation under compressive loading. Butterfly lattice material undergoes a controlled topology transformation when the compressive deformation changes. The transformation enables switching between a bending-dominated and a stretch-dominated topology. The critical transform load and deformation of each stage are obtained by a theoretical model. The failure mode and deformation process are in accordance with the experimental and numerical results. The compressive stress–strain curve from the theoretical and experimental results shows that Butterfly lattice material has more than two stable stress plateaus and has higher specific stiffness and specific strength than the foam material. Finally, effects of topology configuration, cell numbers, and vital geometrical parameters are investigated on the energy absorption property of the Butterfly lattice material.

2. Topological design and fabrication

Butterfly lattice material combined the advantages of lower initial strength of the bending-dominated material and high SEA of stretching-

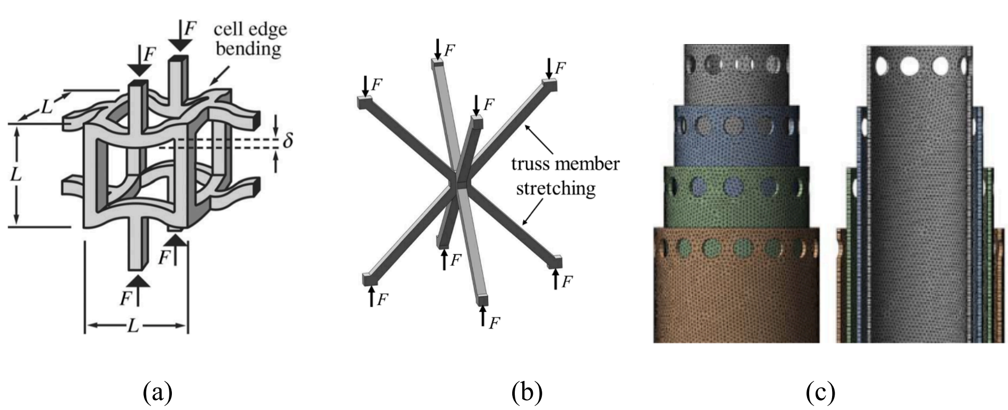

Fig. 2. Three kinds of energy absorption materials or structures (a) bending-dominated materials [43], (b) stretching-dominated lattice materials [43], (c) PEA structure[35].

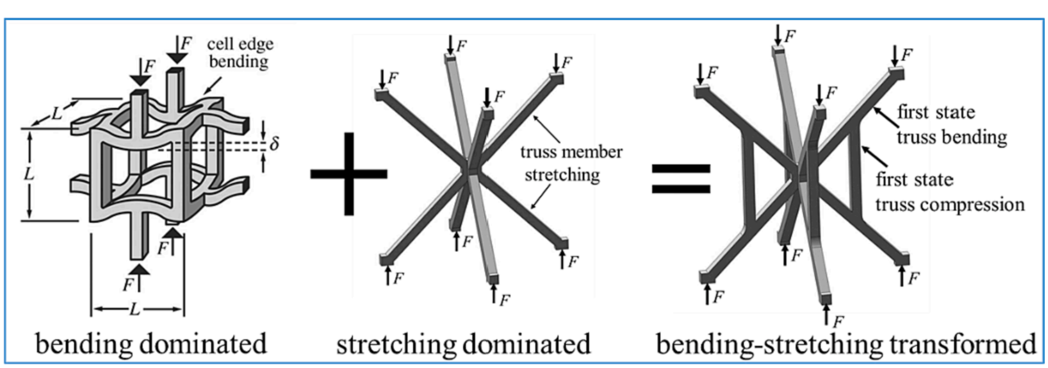

Fig. 3. Design principle of the Butterfly lattice materials.

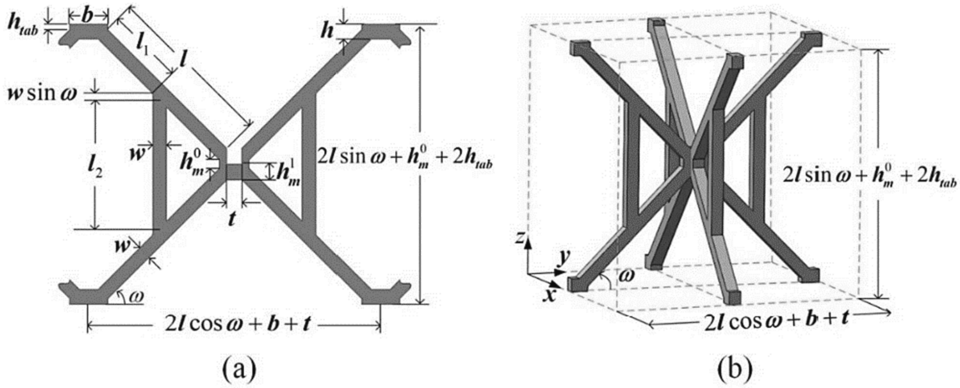

Fig. 4. The schematic diagram of the (a) butterfly truss, (b) unit cell of butterfly lattice.

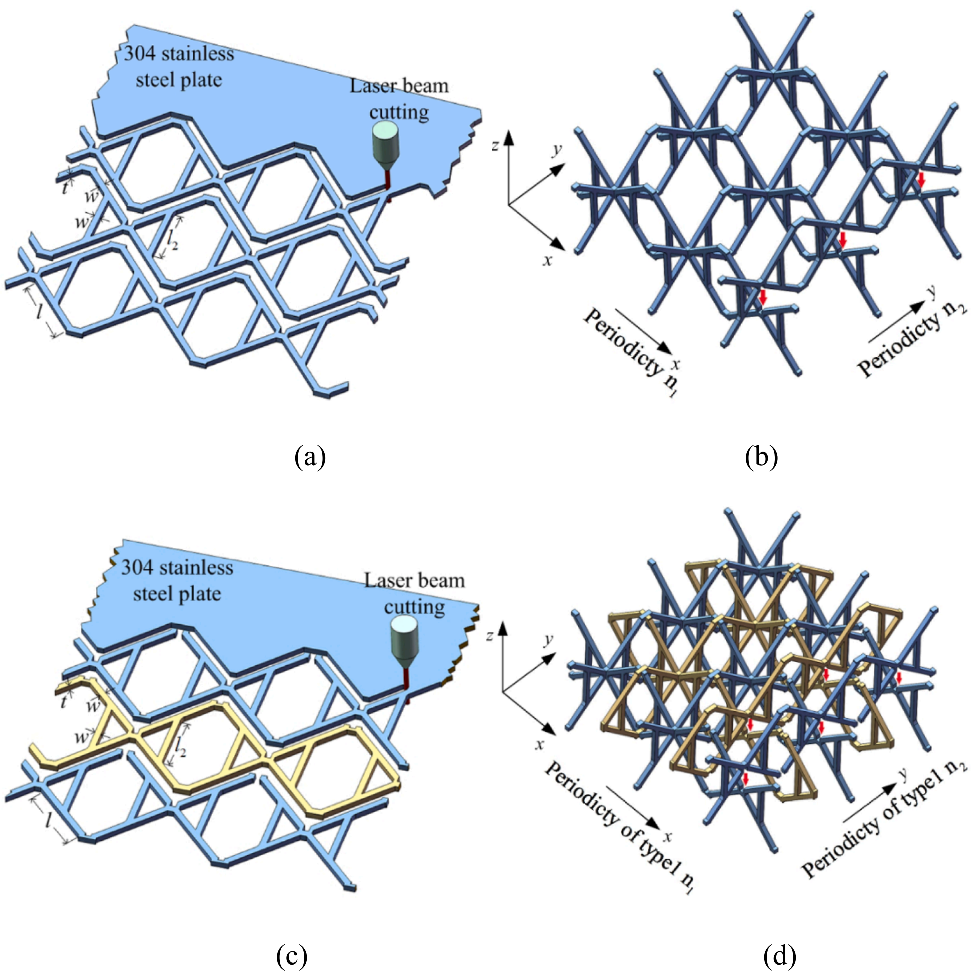

Fig. 5. The fabrication process of Butterfly lattice. The cutting and assembling process of LA Butterfly configuration are shown in (a) and (b), respectively. The cutting and assembling process of TA Butterfly configuration are shown in (c) and (d), respectively.

dominated materials. As shown in Fig. 3, The unit cell of Butterfly lattice is composed of 4 long oblique beams and 4 short vertical beams. The presence of the vertical beams leads the deformation mode of the long-oblique beam to bending from buckling. Therefore, the high initial critical strength and the post-yield softening phenomenon are eliminated. After the bending deformation, the compression load is applied to the vertical short beam. Then the failure modes of the short vertical beam are transformed to buckling, which is stretching-dominated. Fig. 4 shows the schematic diagram of the Butterfly truss. Due to each beam's difference in length and boundary condition, Butterfly lattice material can have multiple failure modes and critical loads.

A snap-fit and vacuum brazing method was used to fabricate the Butterfly cores. The fabrication process mainly includes three steps. Firstly, truss patterns were made from the 304 stainless steel sheets of single thickness with the laser cutting, as shown in Fig. 5(a) and (c). the thickness of the sheet is 1.45 mm; Secondly, these patterns were then snap-fitted into each other to produce a butterfly truss core; Finally, the cores were bonded each other using the vacuum brazing approach. Two

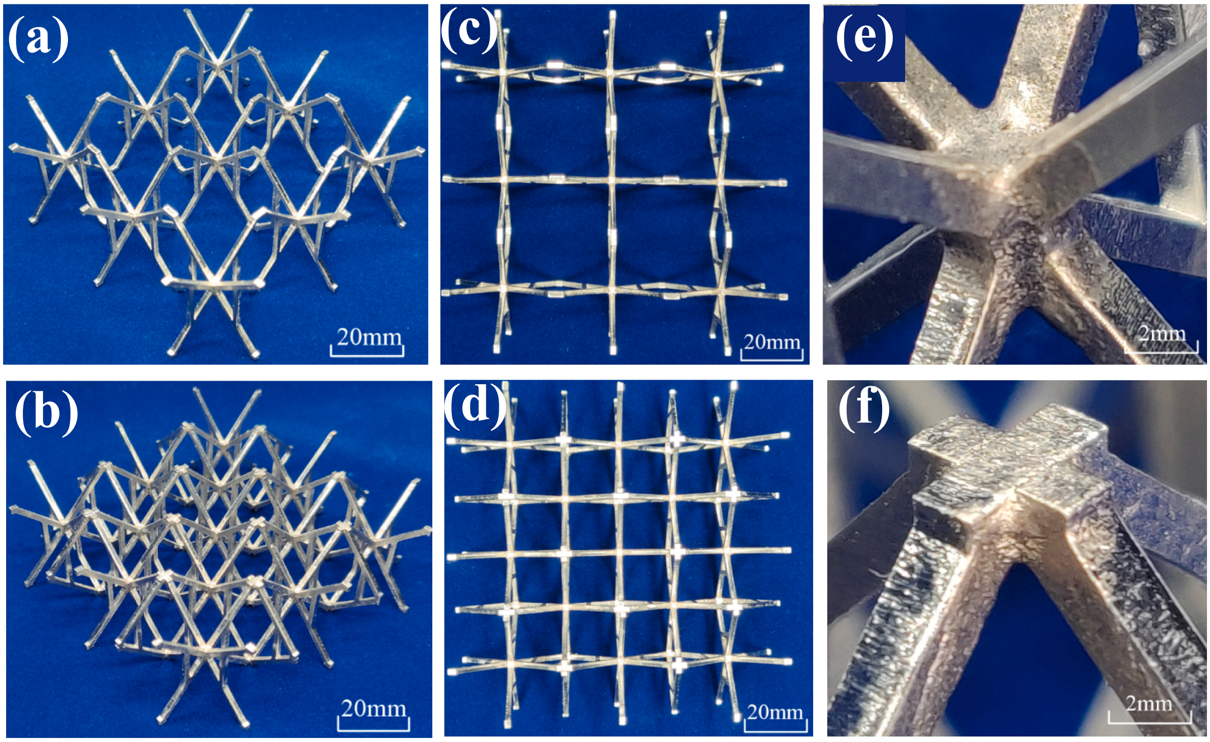

Fig. 6. Photographs of two arrangements of Butterfly lattice structures with relative density, 1.63% and 2.69%. Isometric views of the compressive samples of LA and TA Butterfly configurations are shown in (a) and (b), respectively. The compression loading directions of LA and TA Butterfly configurations are shown in (c) and (d), respectively. The bonded nodes by brazing of LA and TA Butterfly configurations are shown in (e) and (f), respectively.

kinds of arrangements are considered: (1) loose arrangement (LA), the lattice unit cell fitted in alternatively node of the core (Fig. 5(b)). (2) tight arrangement (TA), the lattice unit cell fitted in each node of the core (Fig. 5(d)).

Ni-7Gr-4.5Si-3.1B-3Fe amorphous solder alloy (Nicrobraz 31) was first applied evenly to the nodal regions of the assembled structure. The assembly was placed in a vacuum furnace for high-temperature brazing and heated at 15 °C/min up to 950 °C, held for 30–60 min (to provide a uniform temperature field in the specimens), then heated at 20 °C/min to 1050 °C, for 6 ~ 10 min at 2×10^2 Pa before the furnace naturally cooled to ambient temperature. The two arrangements of of Butterfly truss cores' relative density were about 1.63% and 2.69%, respectively.

3. Theoretical analysis

3.1. Relative density

Geometric parameters of the butterfly lattice member is sketched in Fig. 4, including the oblique beam length l_1, longitude beam length l_2, oblique, and longitude beams width t, thickness w. The relative density $\overline{\rho}_1$, defined as the volume fraction of the volume of the solid material to the total volume in the unit cell, is given by:

$$\overline{\rho}_1 = \frac{8ltw + 4l_2tw + 2t^2h_m^1 + 4bht}{(2l\sin\omega + h_m^0 + 2h_{tab})(2l\cos\omega + b + t)^2} \tag{1}$$

Note that in this paper, the inclination angle of oblique beam with horizontal pale ω is 45° and the cross-sections of all beams are square section, $t = w$. Then, the relative density of the butterfly core can be simplified as:

$$\overline{\rho}_1 = \frac{4(2l + l_2)t^2 + 2t^2h_m^1 + 4bht}{\left(\sqrt{2}\,l + h_m^0 + 2h_{tab}\right)\left(\sqrt{2}\,l + b + t\right)^2} \tag{2}$$

when the node volumes is not considered, the relative density of the ideal butterfly core reduces to:

$$\overline{\rho}_1 = \left(2\sqrt{2} + \sqrt{2}\ \frac{l_2}{l}\right)\left(\frac{t}{l}\right)^2 \tag{4}$$

The relative density of TA B utterfly cores is:

$$\overline{\rho}_2 = N\overline{\rho}_1 \tag{5}$$

$$N = 1 + \frac{(n_1 - 1)(n_2 - 1)}{n_1n_2} \tag{6}$$

Where n_1 and n_2 are the numbers of the LA Butterfly core in the X and Y directions, respectively. When $n_1,\ n_2 >> 1, \rho_2 \approx 2\rho_1$.

3.2. Analysis of multi-stage deformation

The schematic of the multi-stage failure mode is shown in Fig. 7. Butterfly lattice transforms into the substructure from the initial configuration under the compressive load. Two boundary conditions are considered in the theoretical model: free boundary and sliding boundary. A plastic hinge is formed at the intersection of the oblique and the vertical beams for the free boundary condition. For the sliding boundary condition, plastic hinges are formed at the middle of each beam and the intersection of the beams, respectively. The deformation process of this kind of structures have two substructures. As shown in Fig. 7(b), for the first substructure, the main deformation mechanism is the bending of

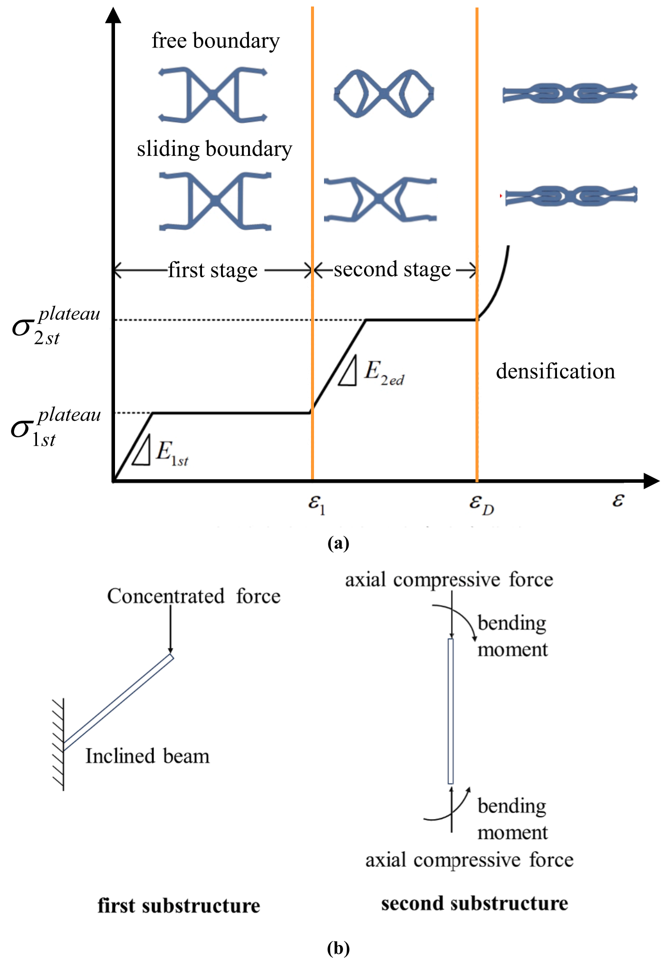

Fig. 7. Schematic of the multi-stage failure mode. (a) progressive stress–strain curve of the unit cell of Butterfly lattice under compression, (b) deformation mechanism.

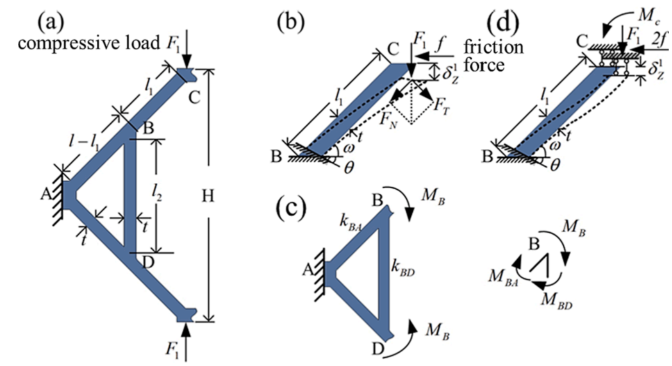

Fig. 8. The force analysis of the first stage of butterfly lattice under compression. (a) one-quarter model of the butterfly unit cell, (b) free of the beam end, (c) guide of the beam end, and (d) the bending distribution of the end nodes of the vertical beam.

the oblique beam. In the second substructure, the main deformation mechanism is the bending of the vertical beam under the compression and bending. Before the first substructure is generated, the post-yield force remains unchanged. After the generation of the second substructure, the compressive stress is increased until a new plastic hinge is formed. Finally, the compressive stress is increased to the third plateau when the two beams are contacted. External compressive load along the Z direction (shown in the coordinate system of Fig. 5) is applied on the Butterfly lattice material. For the lattice material, the compressive load is applied on the point C as F_1 at the first substructure and on the point B as F_2.

3.3. Theoretical analysis of the first stage

According to the deformation of the Butterfly lattice material under the compressive load, the equivalent stiffness can be deduced as (detailed derivation process is in A**ppendix A):

$$E_{1st}^{1}=\frac{4F_1}{A_{cell}\varepsilon_Z}=\frac{E_s t^2 H}{A_{cell}\left[l_1^3+\frac{6l_1^2 l_2(l-l_1)}{4l_2+3(l-l_1)}\right]} \tag{7}$$

Where $A_{cell}=(2l\cos\omega+b+t)^2$ is the cross-sectional area of the lattice cell, F_1 is compressive load applied on the point B, E_s is the elastic modulus of the parent material, I is the moment of inertia of the beam, l_1 is the length of the BC section, H is the total height of the cell.

For the sliding boundary condition, as shown in Fig. 6 (d), the vertical deformation of the beam is

$$\delta_Z^1=\frac{F_T l_1^3}{3E_s I}\cos\omega-\frac{M_C l_1^2}{2E_s I\cos\omega}+\theta_B l_1\cos\omega \tag{8}$$

$$M_C=\frac{1}{2}Fl_1\cos\omega \tag{9}$$

$$E_{1st}^2=2E_{1st}^2 \tag{10}$$

For Butterfly lattice material, both the free and sliding boundaries exist, and the total stiffness is the linear superposition of the two boundary conditions. For LA, the equivalent stiffness can be expressed as

$$E_{1st}=N_1E_{1st}^1+N_2E_{1st}^2=(N_1+2N_2)E_{1st}^1 \tag{11}$$

Where N_1 and N_2 used in are functions of n_1 and $n_{2,}$ and $N_1=\frac{n_1+n_2}{2n_1n_2}$, $N_2=1-N_1$. For lattice material fabricated in this work, $N_1=\frac{1}{3}$, $N_2=\frac{2}{3}$.

For TA, the equivalent stiffness is

$$E_{1st}=N_3E_{1st}^1+N_4E_{1st}^2=(N_3+2N_4)E_{1st}^1 \tag{12}$$

Where $N_3=N_1=\frac{n_1+n_2}{2n_1n_2}$. Due to the different arrangement of the LA and TA configuration, the parameter of N_4 is not the same as N_3, and $N_4=2(1-N_3)$. For lattice material fabricated in this work, $N_3=\frac{1}{3}$, $N_4=\frac{4}{3}$.

The compressive strength of the first stage for the free boundary condition is

$$\sigma_{1st}^{a}=\frac{4F_1^{plateau}}{A_{cell}}=\frac{t^3\sigma_s}{(1-\mu)A_{cell}l_1\cos\omega} \tag{13}$$

For the sliding boundary condition, the bending moment of the point B is

$$M_B=\frac{(1-2\mu)}{2}F_1l_1\cos\omega \tag{14}$$

The compressive strength of point B corresponding to the critical bending moment is

$$\sigma_{1st}^{b}=\frac{2t^3\sigma_s}{(1-2\mu)A_{cell}l_1\cos\omega} \tag{15}$$

For LA Butterfly lattice material, the compressive strength is the linear superposition of the two boundary conditions, which can be expressed as

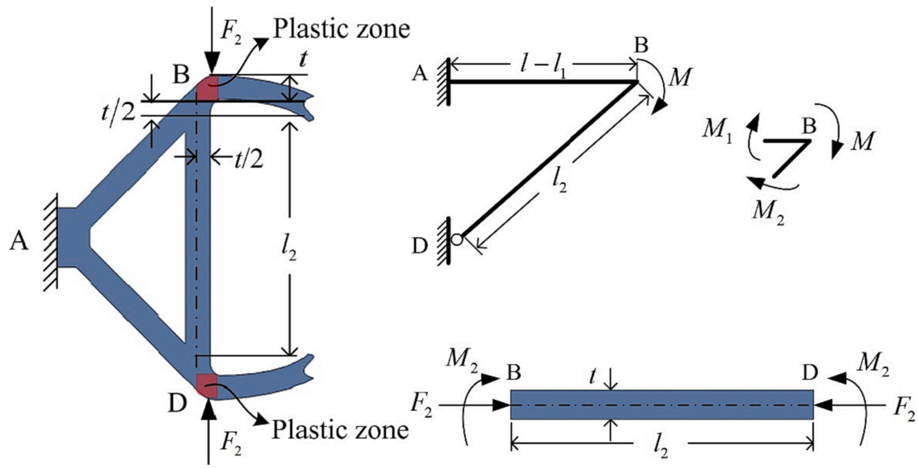

Fig. 9. The force analysis of the second stage of butterfly lattice under compression. (a) one-quarter model of the butterfly daughter configuration, (b) bending distribution at the plastic hinge, (c) the force analysis of vertical bar.

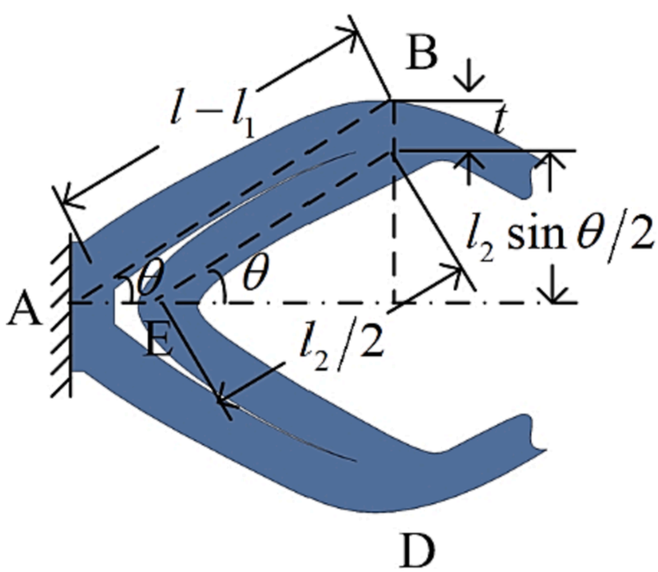

Fig. 10. The geometrical relationship of the truss with densified strain.

$$\sigma_{1st}^{plateau} = N_1\sigma_{1st}^{a} + N_2\sigma_{1st}^{b} \tag{16}$$

When $n_1 = n_2 = 3$,

$$\sigma_{1st}^{plateau} = \frac{1}{3}\sigma_{1st}^{a} + \frac{2}{3}\sigma_{1st}^{b} \tag{17}$$

The compressive strength of the TA Butterfly lattice material is

$$\sigma_{1st}^{plateau} = N_3\sigma_{1st}^{a} + N_4\sigma_{1st}^{b} \tag{18}$$

When $n_1 = n_2 = 3$,

$$\sigma_{1st}^{plateau} = \frac{1}{3}\sigma_{1st}^{a} + \frac{4}{3}\sigma_{1st}^{b} \tag{19}$$

The critical strain of the first stage is

$$\varepsilon_{1st} = \frac{H - l_2 - 3t}{H} \tag{20}$$

3.4. Theoretical analysis on the second stage

According to the deformation of the Butterfly lattice material under the compressive load, as shwon in Fig. 9, the equivalent stiffness of the

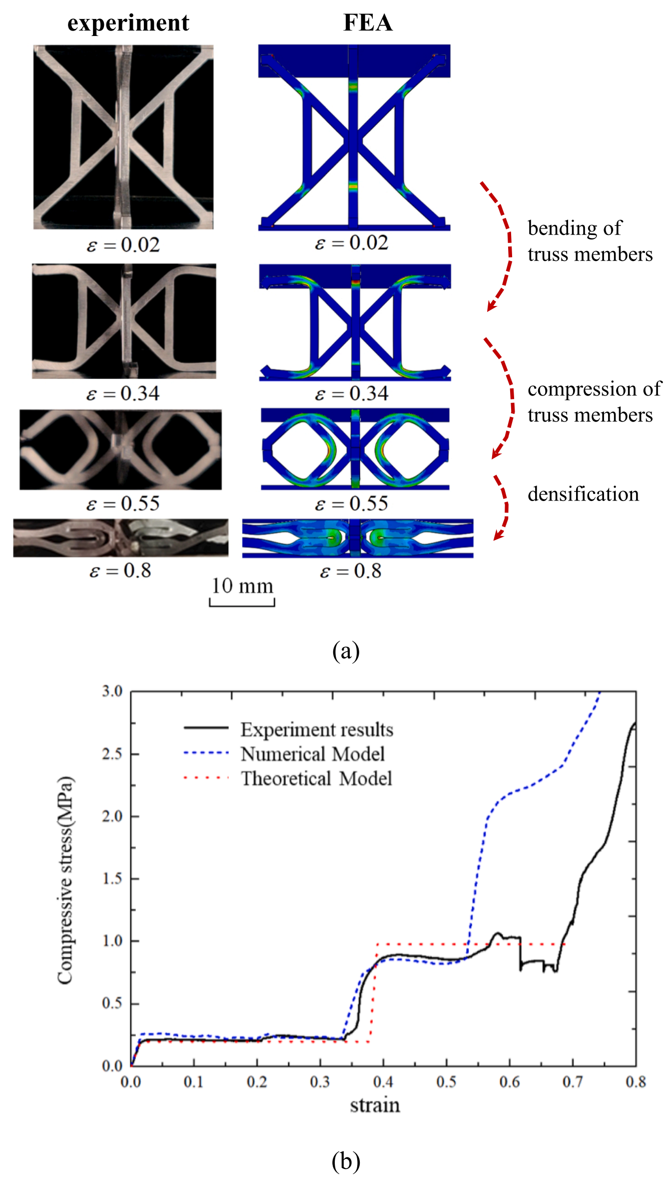

Fig. 11. Compressive deformation results of the butterfly unit cell, (a) Experimental and FEM results and legend of FEM results are equivalent plastic strain. (b) The comparison of the compressive stress–strain curves.

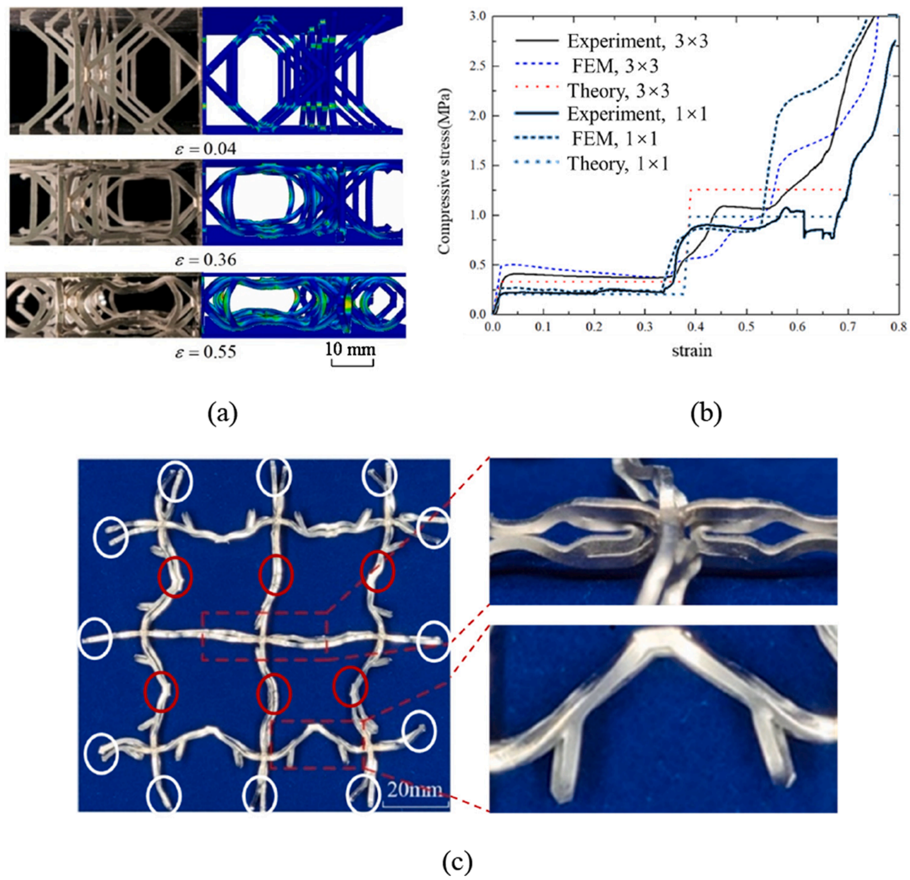

Fig. 12. Compressive deformation results of the butterfly lattice materials with 3 × 3 unit cells. (a) Experimental and FEM results. (b) The compressive stress–strain curves. (c) Beams deformation after quasi-static compression. Regions with white circles are free boundary conditions, and regions with red circles are sliding boundary conditions. (For interpretation of the references to colour in this figure legend, the reader is referred to the web version of this article.

second stage is

$$E_{2ed} = \frac{1}{\Omega}\frac{4t^2}{A_{cell}} \tag{21}$$

$$\Omega = \frac{1}{E_t} + \frac{(l-l_1)(l_2+3t)}{[(l_2+3t)+2(l-l_1)]E_s}$$

The equivalent compressive strength of the second stage for the LA Butterfly lattice material is

$$\sigma_{2nd}^{plateau} = \frac{4F_2^{plateau}}{A_{cell}} = \frac{4\left(\sqrt{L^2(1-k)+k^2}-k\right)}{L^2A_{cell}}t^2\sigma_s \tag{22}$$

Where k is the proportionality coefficient for the bending moment of the beam BC. The equivalent compressive strength of the second stage for the TA Butterfly lattice material is

$$\sigma_{2nd}^{plateau} = N\frac{4F_2^{plateau}}{A_{cell}} = N\frac{4\left(\sqrt{L^2(1-k)+k^2}-k\right)}{L^2A_{cell}}t^2\sigma_s \tag{23}$$

$$N = 2\left(1-\frac{1}{n_1+n_2}\right)$$

Fig. 10 shows the geometrical relationship for the densification of the Butterfly lattice material. Suppose the equivalent stress of the lattice is drastically increased when the beams BE and AB are parallel, then

$$(l-l_1)\sin\theta = \frac{l_2}{2}\sin\theta + t \tag{24}$$

The strain at the beginning of the densification stage is

$$\varepsilon_D = \frac{H-2(l_2\sin\theta/2+t)}{H} = 1-\frac{2t}{H}-\frac{tl_2}{H(l-l_1-l_2/2)} \tag{25}$$

4. Results and discussions

The compressive behavior of Butterfly lattice material was tested experimentally and numerically to verify the precision of the theoretical model. The loading rate is 2 mm/min. A finite element modeling (FEM) is also developed using the commercially available FEM software ABAQUS. The geometrical and material nonlinearities are both considered. The yield strength of the parent material is 225 MPa, the elastic modulus is 210 GPa. The linear strain-hardening is used and the hardening modulus is 3 GPa. Hexahedral scanning element (C3D48R) is used in the model. The surface-to-surface contact condition are used as the contact condition between the loading plate and the beams. The self-contact condition is used as the contact condition among the beams. The number of the mesh along the beam thickness is 5, the mesh number of the

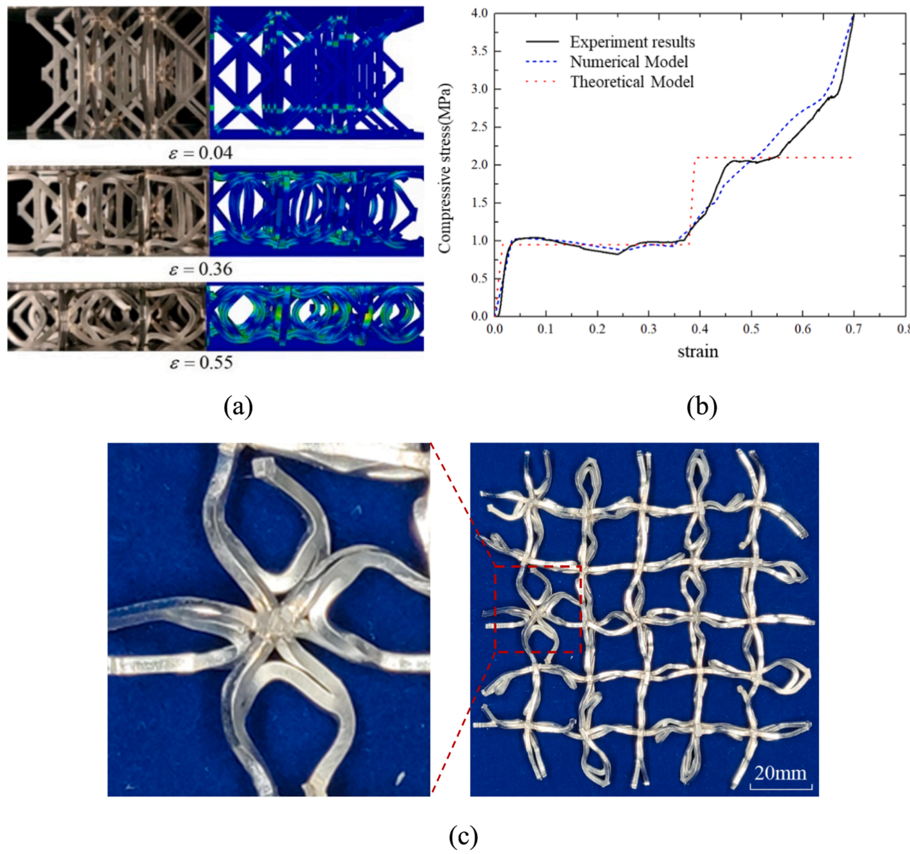

Fig. 13. The experimental and FEM results of the configuration transformation of TA butterfly lattice. (a) Experimental and FEM results. (b) The compressive stress–strain curves. (c) Beams deformation after quasi-static compression.

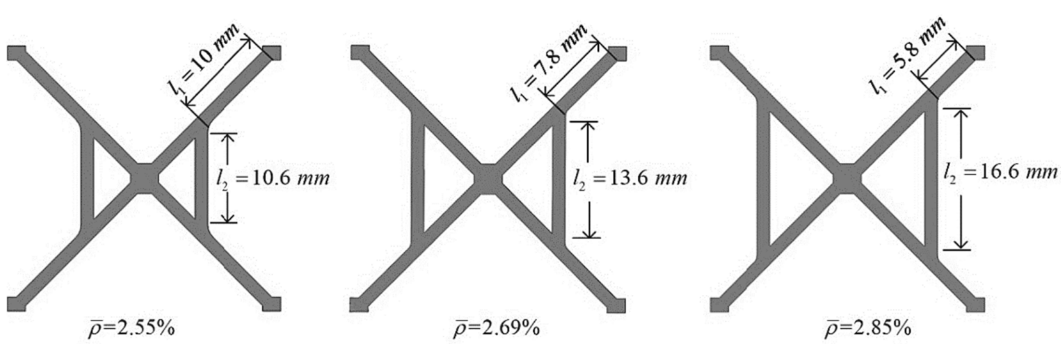

Fig. 14. The butterfly unit cells with three different vertical bars lengths.

oblique beam is about 150 and the total number of the mesh is 22250. The implicit analysis is performed in the model. Then effects of cell numbers, topology configuration, and the main geometrical parameter are investigated on the energy absorption behavior.

4.1. Cell numbers

Fig. 11(a)-(b) show the compressive behavior of the Butterfly lattice material obtained from the experiment and the numerical model. It can be found that the typical substructure, the critical deformation, and the plateau load of each stage obtained from the theoretical model are basically in accordance with that from the experiment and the numerical model. The compressive load arrives at the peak value when the first plastic hinge is formed at the intersection of the oblique and the vertical beams. With the increase of the compressive deformation, the equivalent stress increases to the second peak value when the plastic hinge forms at the middle of the vertical beam. Post-yield softening phenomenon does not occur due to the bending deformation. The two beams are not contacted due to the fabrication error. Therefore, the stress has a slight decline before the densification.

Fig. 12(a) shows the compressive process of the LA Butterfly lattice material with 3 × 3 cells. All the results from the numerical model agree with those from the experiment. Fig. 12(b) shows the compressive stress–strain curves of LA butterfly lattice. The plateau stress of the

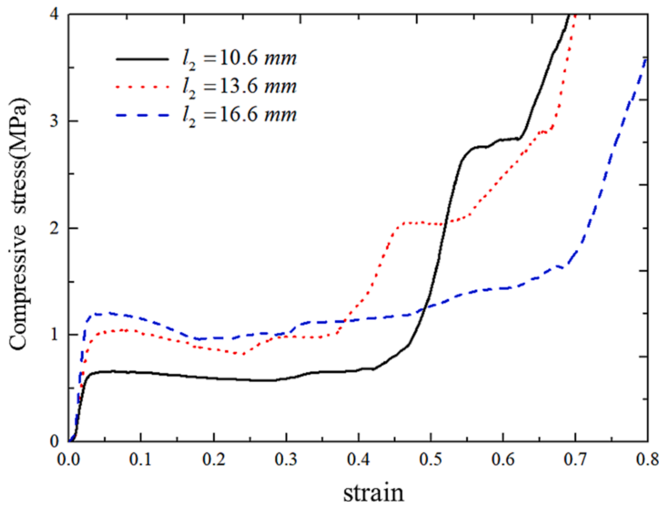

Fig. 15. The compressive stress–strain curves of butterfly lattice of TA with different vertical bar lengths.

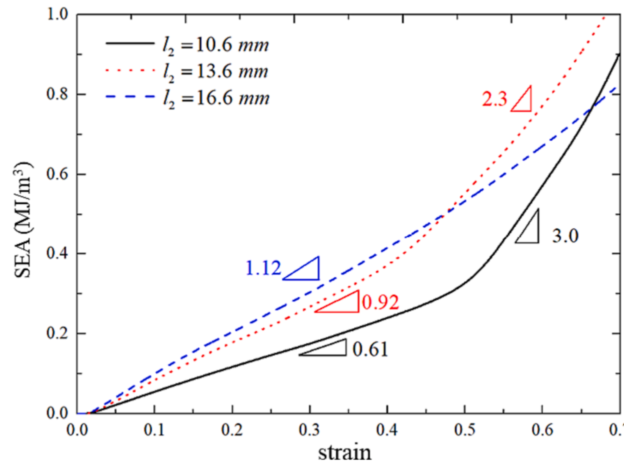

Fig. 16. SEA of the TA butterfly lattice with different vertical bar lengths.

second stage obtained from the theoretical model is bigger than that from the experimental and the numerical due to the bending deformation of the beams in the second substructure. Compared with the compressive behavior of one unit cell, boundary conditions for some of the lattice cells are sliding. The failure mode and critical load are different. All boundary conditions of the central unit cell are sliding. Fig. 12(c) shows the final failure mode in the top view. The surrounding cells have an obvious deformation when the second substructure is formed.

4.2. Topology configuration

TA Butterfly lattice materials are designed to improve the stability of the beams. Fig. 13(a) shows the transforming mode of TA Butterfly lattice under the compressive load. Fig. 13(b) shows the stress–strain curve. All the critical stress and strain of the first stage agree with those from the experiment and the numerical model. In addition, the plateau stress can also be predicted theoretically for the second stage. However, there is no apparent stress plateau in the numerical model and the experiment results in the second stage. In the theoretical model, the stress seems to be constant from the existence of the plastic hinge to the densification stage. Therefore, there is a big difference in the stress between the numerical model and the experiment. Fig. 13(c) shows the failure mode when the compression process is finished. The out-of-plane deformation for the vertical beam of the outside cells is controlled. However, some solder joints are fractured due to the stress concentration.

4.3. Geometrical model

The transform of the geometrical configuration, critical transforming stress, and strain is mainly determined by the position of the plastic hinge, which can be carried out by modifying the length of the vertical beam. The length of vertical beams is 10.6 mm, 13.6 mm, and 16.6 mm, as shown in Fig. 14.

Fig. 15 shows compression results for the butterfly lattice material from the experiment. It is found that the length of the beam has a significant effect on the size of stress and strain plateau. The plateau stress of the first stage decreases with the vertical beam's length increasing, and the second stage's plateau stress increases. When the length of the vertical beam is increased to a particular value, the plateau stress of the first stage equals that of the second stage, and the two stages are merged to a long one. Fig. 16 shows the SEA of the Butterfly lattice materials with different geometrical parameters. It is found that the slope of the SEA is constant at the beginning of the compression process when the vertical beams are 10.6 mm and 13.6 mm, respectively. The slope of the first stage is lower than that of the second stage. For the configuration of 16.6 mm, the SEA is increasing linearly. The energy absorption rate is directly related to the value of the stress plateau. The energy absorption rate is higher when the stress plateau's value increases. Every deformation stage corresponds to one energy absorption rate. When the compression strain is lower than 0.48, the energy absorption capacity of Butterfly lattice material with the vertical beam of 16.6 mm is the maximum among the three configurations. However, the energy absorption capacity of Butterfly lattice material with the vertical beam of 13.6 mm is the maximum when the compression strain is more prominent than 0.48. The comparison of the SEA for Butterfly lattice with those traditional stretching dominated lattice material and bending dominated foam material are shown in Fig. 17. It can be found that even the Butterfly lattice material has a low initial compressive load, the SEA is comparable to the stretching dominated lattice material.

5. Conclusions

A novel multi-stage controllable Butterfly lattice material is presented in this study. The plateau load and plateau deformation of each stage are obtained by the theoretical model and the experiment. Results show that the TA Butterfly lattice material has a more stable deformation process than that of LA type. More than two controllable, gradually increasing stress–strain curves can be obtained by applying vertical beams on the lattice material. Every stage's plateau loads and deformation can be determined by designing the vertical beam length. The Butterfly lattice material is more applicable to the energy absorption system due to its multi-stage controllable deformation, non-post-yield softening, and compressive load increase than the bending-dominated foam and the stretching-dominated lattice material.

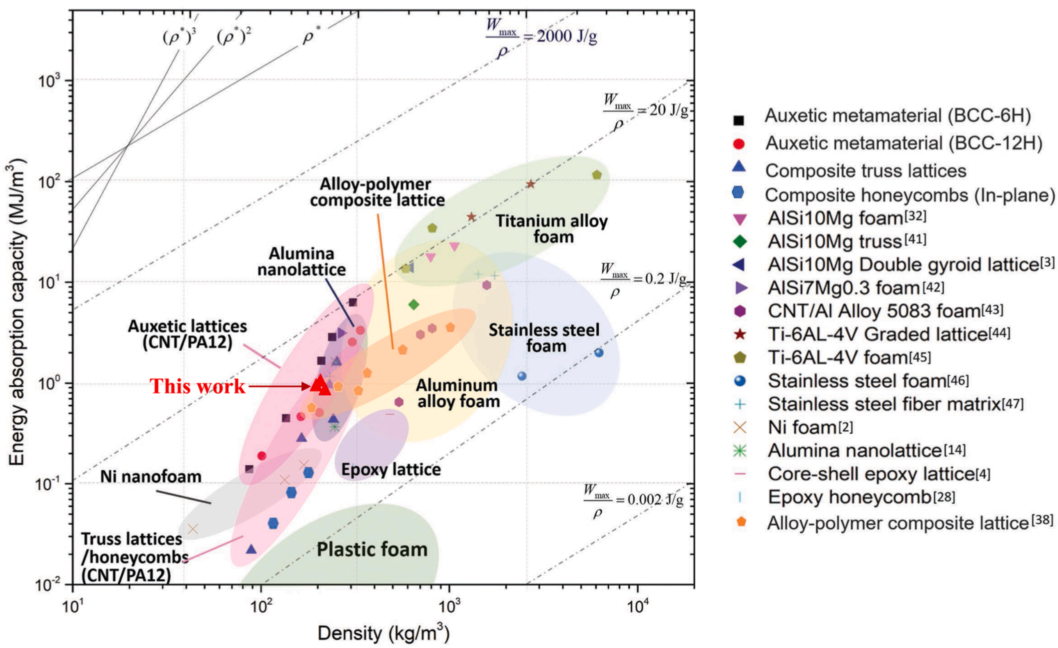

Fig. 17. Ashby map of energy absorption per unit volume versus density. This chart compares the bending-dominated lattice against other most advanced metallic and composite structures so far. The Ashby map is adapted from reference[44].

CRediT authorship contribution statement

Wu Yuan: Data curation, Conceptualization, Investigation, Methodology, Writing – original draft. **Wenfeng Liu:** Conceptualization, Investigation, Methodology. **Hongwei Song:** Conceptualization, Supervision, Writing – review & editing, Funding acquisition. **Chenguang Huang:** Writing – review & editing.

Declaration of Competing Interest

The authors declare that they have no known competing financial interests or personal relationships that could have appeared to influence the work reported in this paper.

Data availability

Data will be made available on request.

Acknowledgments

Financial supports from the National Natural Science Foundation of China (Grant Nos., 11972035, 11972033, 12272379, 11332011, 11902201 and 12172229) are gratefully acknowledged.

Appendix A. . Deformation analysis for the first substructure

The force condition of the lattice is shown in Fig. 8. The vertical force can be divided into axial and tangential forces for the free boundary condition, as shown in Fig. 8(b). The vertical deformation of the beam is

$$\delta_Z^1 = \frac{F_T l_1^3}{3E_s I}\cos\omega + \theta_B l_1 \cos\omega \tag{A.1}$$

θ_B is the angle generated by the bending moment of the point B.

$$F_T = F_1 \cos\omega \tag{A.2}$$

$$M_B = F_1 l_1 \cos\omega \tag{A.3}$$

As shown in Fig. 6(c), the angle of the point B is

$$\theta_B = \frac{2M_B l_2 (l - l_1)\cos\omega}{[4l_2 + 3(l - l_1)]E_s I} \tag{A.4}$$

The equivalent strain of the lattice cell can be shown as

$$\varepsilon_Z = \frac{2\delta_Z^1}{H} \tag{A.5}$$

Appendix B. . Stress analysis for the first substructure

For the free boundary condition, the bending moment of the point B is

$$M_B = (F_1 - f)l_1\cos\omega = (1-\mu)F_1 l_1 \cos\omega \tag{B.1}$$

Where f is the sliding friction force applied on the point C and μ is the coefficient of friction. The critical bending moment when the plastic hinge is completely formed is

$$M_p = \frac{1}{4}t^3\sigma_s \tag{B.2}$$

Accordingly, the plateau fore is

$$F_1^{plateau} = \frac{t^3\sigma_s}{4(1-\mu)l_1\cos\omega} \tag{B.3}$$

Appendix C. . Deformation analysis for the second substructure

The vertical deformation at point B is composed of the elastic deformation of the beam BD δ_Z^e, and the plastic deformation of the plastic hinge δ_Z^p

$$\delta_Z^B = \delta_Z^e + \delta_Z^p \tag{C.1}$$

the elastic deformation of the beam BD is

$$\delta_Z^e = \frac{(l-l_1)(l_2+3t)}{[(l_2+3t)+2(l-l_1)]E_s}\cdot\frac{F_2}{t^2} \tag{C.2}$$

The increment of the plastic strain in the plastic zone is

$$\varepsilon^p = \frac{\Delta\sigma}{E_t} \tag{C.3}$$

The thickness of the plastic zone in the plastic hinge is seen as t. Therefore, the vertical deformation due to the plastic deformation is

$$\delta_Z^p = \frac{F_2}{t^2 E_t} \tag{C.4}$$

Where E_t is the tangential modulus of the parent material.
and

$$\delta_Z^B = \delta_Z^e + \delta_Z^p = \Omega\frac{F_2}{t^2} \tag{C.5}$$

Appendix D. . Stress analysis for the second substructure

Under the combined compressive and bending loads, the strength increased to the second stage when the plastic hinge was formed in the middle of the vertical beam. The bending moment of the beam BC is

$$M_2 = k\left(M_B + M_p\right) = k\left(\frac{1}{2}F_2 t + \frac{1}{4}t^3\sigma_s\right) \tag{D.1}$$

$$k = k_{BD}/(k_{BD}+k_{BA})$$

Under the combined compressive and axial load, the plateau load can be expressed as

$$\frac{M_2}{M_P} + \left(\frac{F_2'}{F_p}\right)^2 = 1 \tag{D.2}$$

Where $M_p = \sigma_s t^3/4$ and $F_p = \sigma_s t^2$ are the plastic bending moment and the plastic compressive load, respectively, F_2' is the axial load of beam BC, then

$$F_2' = LF_2 \tag{D.3}$$

$$L = \frac{2(l-l_1)}{l_2+3t+2(l-l_1)}$$

The plateau compressive load of the second stage is

$$F_2^{plateau} = \frac{\left(\sqrt{L^2(1-k)+k^2} - k\right)}{L^2}t^2\sigma_s \tag{D.4}$$

References

[1] Bhutada S, Goel MD. Crashworthiness parameters and their improvement using tubes as an energy absorbing structure: an overview. Int J Crashworthiness 2021.

[2] Booth DN, Kohar CP, Inal K. Multi-objective optimization of a multi-cellular aluminum extruded crush rail subjected to dynamic axial and oblique impact loading conditions. Thin-Walled Struct 2021;166.

[3] Deshpande VS. Fleck NAJJotM, Solids Po. Energy absorption of an egg-box material 2003;51:187–208.

[4] Hajjari M, Nedoushan RJ, Dastan T, Sheikhzadeh M, Yu WR. Lightweight weft-knitted tubular lattice composite for energy absorption applications: An experimental and numerical study. Int J Solids Struct 2021;213:77–92.

[5] Li WW, Fan HL, Bian YJ, Yang F. Plastic deformation and energy absorption of polycrystalline-like lattice structures. Mater Des 2021;198.

[6] Olabi AG, Morris E, Hashmi MSJ. Metallic tube type energy absorbers: A synopsis. Thin-Walled Struct 2007;45:706–26.

[7] Partovi A, Shahzamanian MM, Wu PD. Numerical study of mechanical behaviour of tubular structures under dynamic compression. J Mech Sci Technol 2021;35:1129–42.

[8] Hajjari M, Nedoushan RJ, Dastan T, Sheikhzadeh M. Yu WRJIJoS, Structures. Lightweight weft-knitted tubular lattice composite for energy absorption applications: An experimental and numerical study; 2020. p. 213.

[9] Huang W, Lu LZ, Fan ZH, Zhang W, Liu JY, Yin CY. Underwater impulsive resistance of the foam reinforced composite lattice sandwich structure. Thin-Walled Struct 2021;166.

[10] Yang LH, Sui L, Dong YL, Li XY, Zi F, Zhang ZX, et al. Quasi-static and dynamic behavior of sandwich panels with multilayer gradient lattice cores. Compos Struct 2021;255.

[11] Yang LH, Sui L, Li XY, Dong YL, Zi F, Wu LZ. Sandwich plates with gradient lattice cores subjected to air blast loadings. Mech Adv Mater Struct 2021;28:1355–66.

[12] Wadley HN. Multifunctional periodic cellular metals. Philos Trans A Math Phys Eng Sci 2006;364:31–68.

[13] V.S. Deshpande NAF, M.F. Ashby.. effective properties of the octet-truss lattice material. J Mech Phys Solids 2001.

[14] Kooistra G. Compressive behavior of age hardenable tetrahedral lattice truss structures made from aluminium. Acta Materialia 2004;52:4229–37.

[15] K. Finnegan GK, H. N. G. Wadley, V. S. Deshpande.. The compressive response of carbon fiber composite pyramidal truss sandwich cores. Int J Mater Res 2007.

[16] Wang J, Evans AG, Dharmasena K, Wadley HNG. On the performance of truss panels with Kagomé cores. Int J Solids Struct 2003;40:6981–8.

[17] Dong L, Deshpande V, Wadley H. Mechanical response of Ti–6Al–4V octet-truss lattice structures. Int J Solids Struct 2015;60–61:107–24.

[18] Feng L-J, Wu L-Z, Yu G-C. An Hourglass truss lattice structure and its mechanical performances. Mater Des 2016;99:581–91.

[19] Albertini F, Dirrenberger J, Sollogoub C, Maconachie T, Leary M, Molotnikov A. Experimental and computational analysis of the mechanical properties of composite auxetic lattice structures. Addit Manuf 2021;47.

[20] Karathanasopoulos N, Dos RF, Reda H, J.-f. g.. Computing the effective bulk and normal to shear properties of common two-dimensional architectured materials. Computational Materials ence 2018;154:284–94.

[21] Tancogne-Dejean T, Karathanasopoulos N, Mohr D. Stiffness and Strength of Hexachiral Honeycomb-Like Metamaterials. J Appl Mech 2019;86:1–38.

[22] Dos Reis F, Ganghoffer JF. Homogenized elastoplastic response of repetitive 2D lattice truss materials. Computational Materials ence 2014;84:145–55.

[23] Goda I, Reis FD, Limit GJF. Analysis of Lattices Based on the Asymptotic Homogenization Method and Prediction of Size Effects in Bone Plastic Collapse. Springer International Publishing; 2016.

[24] Holm Altenbach SF. Generalized Continua as Models for Classical and Advanced Materials: Springer Cham, 2016.

[25] Ashby MF. The properties of foams and lattices. Philos Trans A Math Phys Eng Sci 2006;364:15–30.

[26] Deshpande VS, Fleck NA. Energy absorption of an egg-box material. J Mech Phys Solids 2003;51:187–208.

[27] Evans AG, He MY, Deshpande VS, Hutchinson JW, Jacobsen AJ, Carter WB. Concepts for enhanced energy absorption using hollow micro-lattices. Int J Impact Eng 2010;37:947–59.

[28] Pingle SM, Fleck NA, Deshpande VS, Wadley HNG. Collapse mechanism maps for a hollow pyramidal lattice. Proceedings of the Royal Society A: Mathematical, Physical and Engineering Sciences. 2010;467:985-1011.

[29] Dharmasena KP, Queheillalt DT, Wadley HNG, Dudt P, Chen Y, Knight D, et al. Dynamic compression of metallic sandwich structures during planar impulsive loading in water. Eur J Mech A Solids 2010;29:56–67.

[30] Wadley H, Dharmasena K, Chen Y, Dudt P, Knight D, Charette R, et al. Compressive response of multilayered pyramidal lattices during underwater shock loading. Int J Impact Eng 2008;35:1102–14.

[31] Lorna J, Gibson MFA. Cellular Solids: Structures and Properties 1997.

[32] Qin QH, Wang TJ. Low-velocity heavy-mass impact response of slender metal foam core sandwich beam. Compos Struct 2011;93:1526–37.

[33] Yu JL, Wang EH, Li JR, Zheng ZJ. Static and low-velocity impact behavior of sandwich beams with closed-cell aluminum-foam core in three-point bending. Int J Impact Eng 2008;35:885–94.

[34] Zahran MS, Xue P, Esa MS, Abdelwahab MM. A novel tailor-made technique for enhancing the crashworthiness by multi-stage tubular square tubes. Thin-Walled Struct 2018;122:64–82.

[35] Esa M, Xue P, Zahran M, Abdelwahab M, Khalil M. Novel strategy using crash tubes adaptor for damage levels manipulation and total weight reduction. Thin-Walled Struct 2017;111:176–88.

[36] Kotełko M, Ferdynus M, Jankowski J. Energy Absorbing Effectiveness – Different Approaches. Acta Mechanica et Automatica 2018;12:54–9.

[37] Xu P, Yang C, Peng Y, Yao S, Zhang D, Li B. Crash performance and multi-objective optimization of a gradual energy-absorbing structure for subway vehicles. Int J Mech Sci 2016;107:1–12.

[38] Cetin E, Baykasoglu C. Energy absorption of thin-walled tubes enhanced by lattice structures. Int J Mech Sci 2019;157:471–84.

[39] Lykakos S, Kostazos PK, Manolakos DE. Quasi-static axial crushing of thin-walled steel tapered tubes with hybrid geometry: experimental and numerical investigation. Int J Crashworthiness 2020.

[40] Magrinho JP, Centeno G, Silva MB, Vallellano C, Martin PAF. On the formability limits of thin-walled tube inversion using different die fillet radii. Thin-Walled Struct 2019;144.

[41] Taghipoor H, Eyvazian A, Ghiaskar A, Kumar AP, Hamouda AM, Gobbi M. Experimental investigation of the thin-walled energy absorbers with different sections including surface imperfections under low-speed impact test. Materials Today-Proceedings 2020;27:1498–504.

[42] Zhang X, Zhang H, Yang CY, Leng KH. Static and dynamic axial crushing of self-locking multi-cell tubes. Int J Impact Eng 2019;127:17–30.

[43] Ashby P. MFJPTM, Sciences E. The properties of foams and lattices 2006;364:15–30.

[44] Yuan S, Chua CK, Zhou KJAMT. 3Dccrinted Mechanical Metamaterials with High Energy Absorption. 2018;4.